SCIENCE CHINA Materials ARTICLES

mater.scichina.com link.springer.com

Published online 11 September 2020 | https://doi.org/10.1007/s40843-020-1430-4
Sci China Mater 2020, 63(11): 2261–2271

SPECIAL TOPIC: Advanced Photocatalytic Materials

Sol-gel synthesis of highly reproducible WO_3 photoanodes for solar water oxidation

Jianyong Feng[1†], Xin Zhao[1†], Bowei Zhang[1], Guang Yang[1], Qinfeng Qian[2], Su Su Khine Ma[1], Zhong Chen[1], Zhaosheng Li[2*] and Yizhong Huang[1*]

ABSTRACT **Although monoclinic WO_3 is widely studied as a prototypical photoanode material for solar water splitting, limited success, hitherto, in fabricating WO_3 photoanodes that simultaneously demonstrate high efficiency and reproducibility has been realized. The difficulty in controlling both the efficiency and reproducibility is derived from the ever-changing structures/compositions and chemical environments of the precursors, such as peroxytungstic acid and freshly prepared tungstic acid, which render the fabrication processes of the WO_3 photoanodes particularly uncontrollable. Herein, a highly reproducible sol-gel process was developed to establish efficient and translucent WO_3 photoanodes using a chemically stable ammonium metatungstate precursor. Under standard simulated sunlight of air mass 1.5 G, 100 mW cm^{-2}, the WO_3 photoanode delivered photocurrent densities of ca. 2.05 and 2.25 mA cm^{-2} at 1.23 V *versus* the reversible hydrogen electrode (RHE), when tested in 1 mol L^{-1} H_2SO_4 and CH_3SO_3H, respectively. Hence, the WO_3 photoanodes fabricated herein are one of the WO_3 photoanodes with the highest performance ever reported. The reproducibility of the fabrication scheme was evaluated by testing 50 randomly selected WO_3 samples in 1 mol L^{-1} H_2SO_4, which yielded an average photocurrent density of 1.8 mA cm^{-2} at 1.23 V_{RHE} with a small standard deviation. Additionally, the effectiveness of the ammonium metatungstate precursor solution was maintained for at least 3 weeks, when compared with the associated upper-limit values of peroxytungstic and tungstic acid-based precursors after 3 d. This study presents a key step to the future development of WO_3 photoanodes for efficient solar water splitting.**

Keywords: solar water splitting, WO_3, photoanode, sol-gel process, photoelectrochemical cell

INTRODUCTION

By converting solar energy, the largest renewable energy source on the planet, into storable and clean chemical fuels, artificial photosynthesis offers an elegant way to achieve a fully sustainable society [1–5]. Among various artificial photosynthesis systems, water splitting by photoelectrochemical (PEC) cells has attracted considerable interest since the seminal work on TiO_2 photoelectrodes [6]. To maximize the utilization of the solar spectrum, numerous visible-light-responsive semiconductors have been explored as photoelectrodes for solar water splitting, such as (oxy)nitrides [7–10], and chalcogenides [11]. However, metal oxide semiconductors, such as $BiVO_4$ [12,13], Fe_2O_3 [14,15], and Cu_2O [16], remain the state-of-the-art materials within the PEC field, since metal oxide semiconductors exhibit relatively high chemical stability in aqueous solutions, and are easy to fabricate whilst naturally occurring in abundance within the crust of the Earth [17–19]. Among these key transition-metal oxide semiconductors, monoclinic WO_3 has received a wealth of interdependent research as a result of having a visible spectrum sensitivity up to 470 nm, photostability in acidic solutions, high electron mobility, and a relatively long hole diffusion length of ca. 150 nm [20–22].

Extensive research efforts have led to numerous synthetic strategies to produce efficient and translucent WO_3 photoanodes, for example, by electrodeposition [20], sol-gel [23], sputtering [24], hydrothermal [25,26], and solvothermal methods [27]. In terms of efficiency losses occurring through optical absorption, charge transport and surface catalysis processes of the WO_3 photoanodes,

[1] School of Materials Science and Engineering, Nanyang Technological University, Singapore 639798, Singapore
[2] Collaborative Innovation Center of Advanced Microstructures, National Laboratory of Solid State Microstructures, College of Engineering and Applied Sciences, Nanjing University, Nanjing 210093, China
[†] These authors contributed equally to this work.
[*] Corresponding authors (emails: zsli@nju.edu.cn (Li Z); yzhuang@ntu.edu.sg (Huang Y))

various strategies have been developed to minimize the losses, including morphology control of the nanostructured electrodes (such as nanorods [25], nanoflakes [28–31], and nanoporous films [23,32]), heterojunction construction [33,34], and electrocatalyst decoration [35–37]. Despite the progress hitherto, establishing efficient and highly reproducible WO_3 photoanodes remains a challenge. The discrepancy in the reproducibility can be understood by the fact that the majority of the previous studies apply peroxytungstic acid and freshly prepared tungstic acid as the precursors, where the precursor structures/compositions and chemical environments change as a function of time, thereby leading to poor reproducibility of the resulting WO_3 photoanodes with respect to film quality and PEC performance. In this regard, there is an urgent need to develop a facile and yet highly reproducible fabrication scheme for WO_3 photoanodes.

Compared with peroxytungstic acid and freshly prepared tungstic acid, ammonium metatungstate (AMT) is relatively stable under ambient conditions. In previous reports, AMT aqueous solutions (with added organic/inorganic acids or surfactants) were hydrothermally treated to generate WO_3 nanopowders, which were processed into pastes for WO_3 electrode fabrication [38–40]. Conversely, ultrasonic spray pyrolysis of AMT aqueous solutions [41], and dip-/spin-coating of aqueous sols comprising AMT and polymer additives [42–45] were employed to deposit WO_3 thin films on various substrates, including glass, fluorine-doped tin oxide (FTO), and polished alumina substrates. Herein, by establishing a modified sol-gel process in which chemically stable AMT was used as the precursor, the above-mentioned challenge related to enhancing the reproducibility of WO_3 photoanodes is circumvented. By adopting this modified procedure, translucent and efficient WO_3 photoanodes that exhibit a high degree of reproducibility are readily realized. Additionally, compared with the classic peroxytungstic acid- and tungstic acid-based precursors, which only retain a high degree of effectiveness for no more than 3 d, AMT-derived precursor solutions continued to produce efficient and reproducible WO_3 photoanodes for at least 3 weeks. This study, therefore, provides a facile but effective route to construct highly efficient WO_3-based PEC water-splitting devices.

EXPERIMENTAL SECTION

Fabrication of WO_3 photoanodes

WO_3 photoanode films were fabricated by using a modified sol-gel method. The precursor solution was prepared by dissolving 0.5 mmol tungsten in the form of ammonium metatungstate hydrate (≥66.5% based on W, Aldrich) in 4.7 mL ethylene glycol (99.8%, Aldrich), following which 1 mmol fumaric acid (≥99.0%, Fluka) and 0.3 mL HNO_3 (min. 69%, Honeywell) were added. After sonication, a clear solution was obtained, and the solution was aged for 24 h before use. The above precursor solution (20 μL) was dropped onto FTO glass substrates (1 cm × 1 cm of the coated area), and dried on a hot plate at 90°C for 20 min and then at 120°C for another 20 min. The films were then annealed for 20 min in a box furnace (Nabertherm, W × D × H: 90 × 115 × 110 mm^3) that had been preheated to 650°C. Four consecutive deposition-annealing cycles were needed to achieve a final ca. 3-μm-thick WO_3 film. Different annealing temperatures (500, 550, 600, 700 °C) were also applied to fabricate WO_3 photoanode films, with the annealing time of 20 min for 700°C and 1 h for other temperatures.

Electrochemical characterizations

PEC measurements were carried out in a three-electrode configuration cell, with WO_3 films as the working electrodes, a Ag/AgCl electrode in saturated KCl as the reference electrode, and a Pt foil as the counter electrode. The electrolyte was a 1 mol L^{-1} H_2SO_4 aqueous solution. Potentials were reported *vs.* the reversible hydrogen electrode (RHE) unless noted otherwise. Photocurrent densities were recorded under AM 1.5 G simulated sunlight (100 mW cm^{-2}), from an Asahi HAL-320 EX3 simulator. The light intensity of the sunlight simulator was calibrated at 100 mW cm^{-2} by the standard reference of a Newport 91150V silicon cell before use. The irradiated area was a circle with a diameter of ca. 6 mm. The incident photon to current efficiency (IPCE) was measured under monochromatic light irradiation, provided by the xenon lamp equipped with band pass filters. The light intensity was obtained with a photometer (Newport, 840-C).

Sample characterizations

The crystal structures of all the samples were measured by thin film X-ray diffraction (XRD, Shimadzu LabX-XRD-6000) with Cu Kα radiation (λ = 1.5418 Å). The optical absorption spectra of the thin film samples were obtained on an UV–visible–near-infrared (UV–Vis–NIR) spectrophotometer (PerkinElmer, Lambda 950). The morphology of the thin film samples was observed by field-emission scanning electron microscopy (FE-SEM; JEOL,

JSM-7600F), and no conductive coating was deposited onto the samples for the SEM measurements.

RESULTS AND DISCUSSION

Sol-gel synthesis and PEC behaviors of WO_3 photoanodes

The precursor solution for the sol-gel processing of the WO_3 films was formed by dissolving AMT, fumaric acid and HNO_3 in ethylene glycol. Upon dropping onto an FTO substrate and heating on a hot plate, the esterification reaction between fumaric acid and ethylene glycol occurred in the precursor solution, forming a transparent gel layer. Thereafter, the gel films were annealed in a box furnace to produce pale yellow WO_3 films that adhere well to the FTO glass substrates. The associated reaction process for the sol-gel production of the WO_3 films is schematically illustrated in Scheme 1. On the basis of annealing temperatures, the as-obtained WO_3 films are denoted as WO_3 500, WO_3 550, WO_3 600, WO_3 650 and WO_3 700, respectively. The annealing time for WO_3 500, WO_3 550 and WO_3 600 films was 1 h, and for the WO_3 650 and WO_3 700 films, the annealing time was reduced to 20 min, to minimize the undesirable damages to the FTO glass substrates.

Fig. 1a shows the current–potential curves of different WO_3 photoanodes in a 1 mol L^{-1} H_2SO_4 aqueous solution under dark and air mass 1.5 G simulated sunlight (100 mW cm^{-2}). Across the potential range of 0.6–2.1 V_{RHE}, all WO_3 photoanodes exhibit dark current densities <0.02 mA cm^{-2}. At negative potentials of 0.6 V_{RHE}, obvious capacitive currents are observed, which decrease gradually as a function of increased annealing temperature of the WO_3 photoanodes. Under simulated sunlight illumination, water splitting photocurrents on the WO_3 photoanodes increase steadily when the applied potentials exceed 0.7 V_{RHE}. By analyzing the PEC response of each WO_3 photoanode, there is a clear trend that continuous and appreciable performance improvements occur with the increase of WO_3 photoanode annealing temperature from 500 to 650°C, followed by an abrupt decrease in photoactivity beyond 650°C (Fig. 1b). This phenomenon can be partially rationalized by the improved crystallinity of WO_3 at higher temperatures, as confirmed by XRD measurements (Fig. 1c and d). All WO_3 photoanodes show XRD patterns having a preferred (200) orientation, as manifested by the highest peak intensity at ~24.3°.

However, improved crystallinity does not always guarantee further improvements in photoactivity, as exemplified by the WO_3 600 (annealing time 1 h) and WO_3 700 photoanodes, which exhibit higher XRD peak intensities but inferior performances when compared with the WO_3 650 photoanode (annealing time 20 min), as shown in Fig. 1b. Because multiple processes occur during the heating procedure (e.g., crystallization, particle growth and coalescence, defect formation and elimination), the above observations suggest that, besides crystallinity, other factors may also influence the performance of the WO_3 photoanodes. The film particle size is one of these factors, in view of the appearances and transmission spectra of the WO_3 films obtained at different temperatures (Fig. S1). Furthermore, the trade-off between crystallinity and particle size is well documented in the literature [46]. Inter-particle connectivity and film porosity, which affect the transport pathways of the majority of charge carriers and collection of minority charge carriers, respectively, are suggested to be the other two contributing factors [23,47].

The above hypotheses are supported by the SEM images, as shown in Fig. 2. For the WO_3 films synthesized at

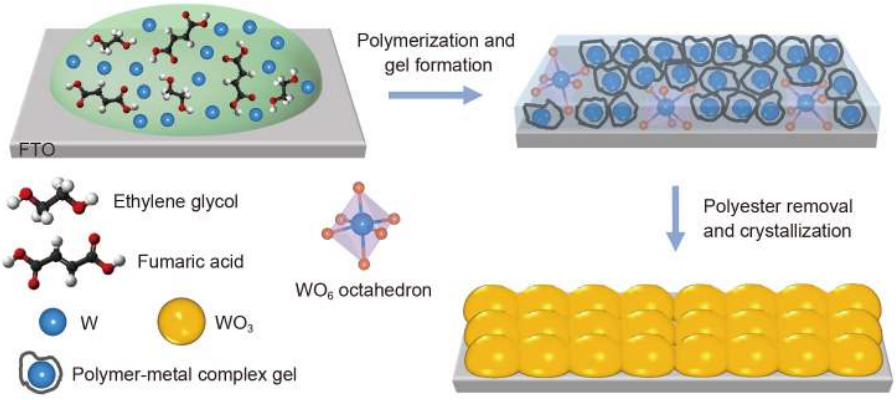

Scheme 1 Schematic illustration of the sol-gel production of WO_3 films.

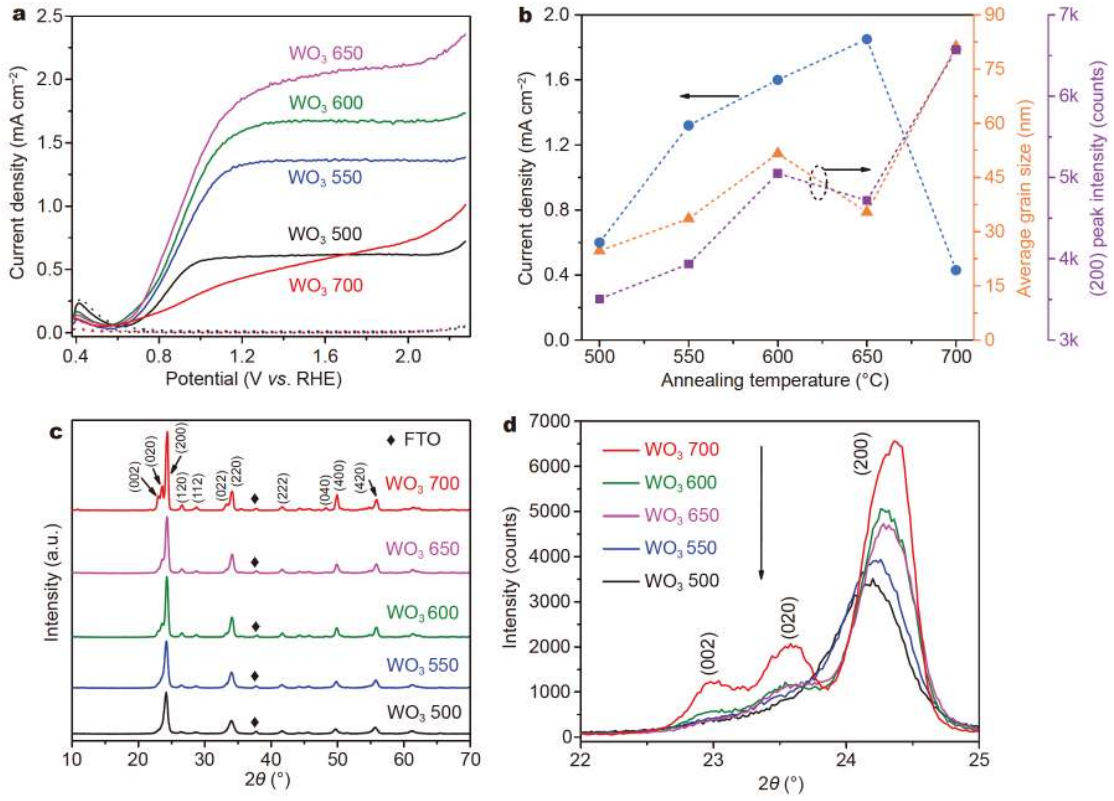

Figure 1 PEC and structural properties of the WO_3 photoanodes. (a) Current–potential curves of WO_3 photoanodes synthesized at different temperatures in dark (dotted lines) and under AM 1.5G 100 mW cm^{-2} simulated sunlight (solid lines). (b) Photocurrent densities at 1.23 V_{RHE}, average grain sizes, and (200) peak intensities of WO_3 photoanodes as a function of annealing temperature. The electrodes were illuminated from the front side, the electrolyte was a 1 mol L^{-1} H_2SO_4 aqueous solution, and the scan rate was 30 mV s^{-1}. (c, d) XRD patterns of the WO_3 films synthesized at different temperatures.

low temperatures (500 and 550°C), the favorable hole transport endowed by their porous structures and small particle sizes could be canceled/weakened by the poor electron transport that originates from loosely aggregated film particles and poor crystallinity. The photocurrent difference between front-side and back-side illumination can give an indication of which process (electron or hole transport) limits/dominates the photoelectrode performance [48]. As shown in Fig. S2, for the WO_3 films synthesized at low temperatures (500 and 550°C), back-side illumination yielded significantly higher photocurrents at high potentials, indicating that poor electron transport limits the water splitting performances; such findings are in good agreement with the above analyses on the WO_3 500 and WO_3 550 electrodes. Upon elevating the annealing temperature, the bottleneck associated with poor electron transport in WO_3 is gradually ameliorated (for WO_3 600, WO_3 650 and WO_3 700 films), as evidenced by the comparable, or even higher, photocurrents observed from front-side illumination than that of back-side illumination. As discussed above, the enhanced electron transport in the WO_3 600, WO_3 650 and WO_3 700 photoanodes relates to the increased crystallinity, particle sizes and inter-particle connectivity (Fig. 1b). However, annealing WO_3 at 700°C leads to an abrupt development of particles comprising large grains; under such conditions, poor hole transport, because of reduced film porosity, largely dominates the overall WO_3 700 performance, despite good electron transport ensured by firmly interconnected film particles (as a result of particle growth and coalescence at high temperatures) and high crystallinity. For the WO_3 electrode formed at 650°C, the highly crystalline interconnected film particles facilitates efficient electron transport to the FTO substrate; conversely, the relatively small average particle size of WO_3 650, as compared with WO_3 600 and WO_3 700 (35.4 nm *vs.* 51.6 and 81.2 nm), as well as a slightly porous structure, favors the hole transport to the electrolyte. Therefore, among all the samples, the WO_3 650 photoanode optimizes crystallinity, inter-particle connectivity, film

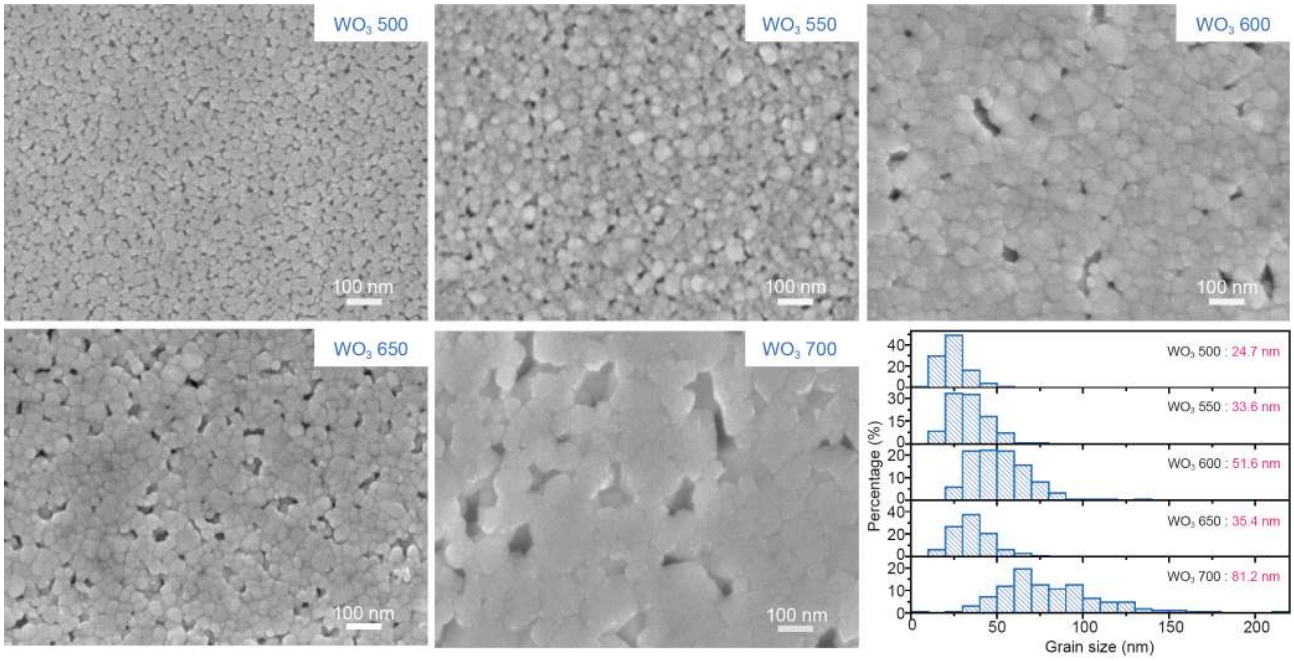

Figure 2 SEM images, grain size distributions and mean grain sizes of the WO_3 films synthesized at different temperatures.

porosity and particle size, by which efficient electron and hole transport are both enhanced. As such, the WO_3 650 electrode exhibits the highest photoactivity among all the WO_3 photoanodes, and the saturation photocurrent of ca. 2.1 mA cm^{-2} renders WO_3 650 among the most efficient WO_3 photoanodes reported in the literature.

Effects of film thickness and precursor solution components on PEC behaviors of WO_3 photoanodes

The effects of film thickness on PEC water splitting for the WO_3 650 photoanodes are presented in Fig. 3a. By increasing the WO_3 650 film thickness, the photocurrents are gradually increased (Fig. 3b). The best-performing WO_3 650 photoanode is formed by four consecutive deposition-annealing cycles, corresponding to a total film thickness of ca. 3 μm (Fig. 3c). Further enhancements in photoactivity might be attainable by employing thicker (>3 μm) WO_3 650 films, but cracks form when the fifth layer is applied; this is deleterious for the operation of the WO_3-based tandem cells because of the reduced WO_3 film transparency. Furthermore, the present 3-μm WO_3 650 film is already sufficiently thick to harvest the majority of the above-bandgap photons, as confirmed by the light harvesting efficiency spectrum (Fig. S3). As front-side illumination always produces higher photocurrents than back-side illumination for WO_3 650 photoanodes regardless of the film thickness (Fig. S4), the data suggest that hole transport dominates the WO_3 650 photoelectrode performance. The relatively poor hole transport observed in the WO_3 650 photoelectrodes is partially a result of a limited film porosity, as shown in Fig. 3c.

Experiments were also undertaken to investigate the influence of the precursor solution composition on the WO_3 photoanode performance. As shown in Fig. 4, removing one or two constituents in the precursor solution, or replacing HNO_3 with HCl, resulted in less effective WO_3 photoanodes. Conversely, both reducing and increasing the fumaric acid concentration in the precursor solution lead to suppressed photocurrents (Fig. 5). The experimental observations with SEM and XRD analyses (Fig. 5 and Fig. S5) suggest that each precursor constituent in the solution plays a unique role in determining the morphology and photoactivity of the resulting WO_3 films. In addition to functioning as a solvent, ethylene glycol also acts as a reactant along with fumaric acid to form the three-dimensionally interconnected ester network, by which the formation and growth of WO_3 particles during annealing are confined to a specific volume. Without fumaric acid, the consequent organic ester template fails to form, leading to an abrupt increase in the WO_3 particle size, as revealed by Fig. 4b and c. A small amount of HNO_3 added into the precursor solution functioned as a catalyst to promote the esterification reaction. Eliminating HNO_3, or replacing HNO_3 with HCl,

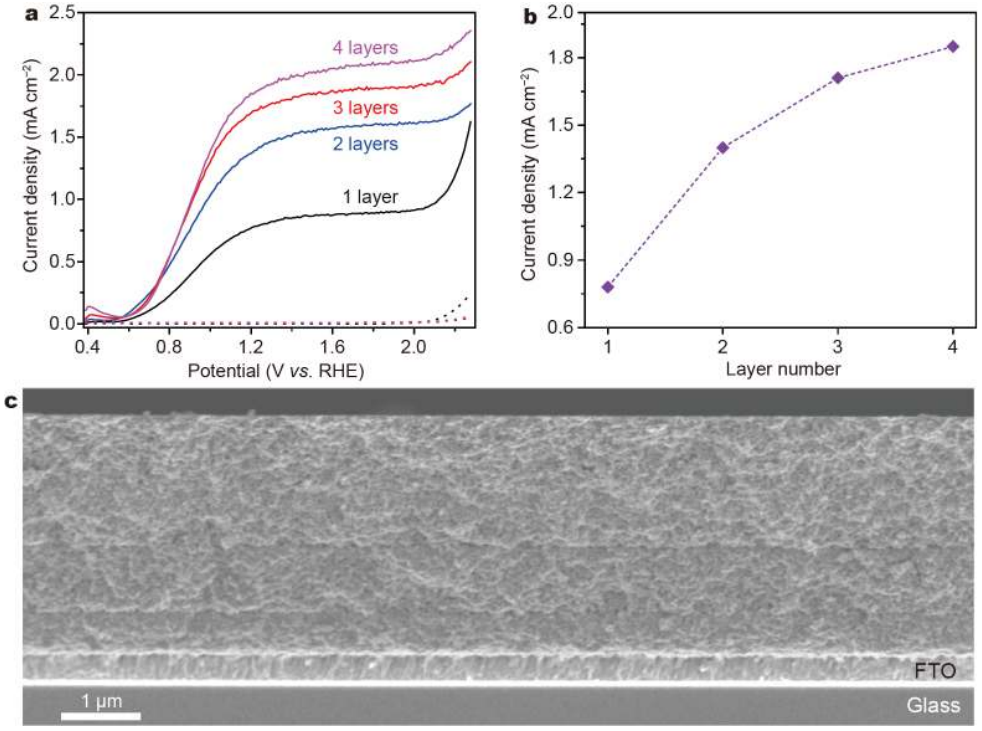

Figure 3 PEC and morphological properties of the WO_3 photoanodes synthesized at 650°C. Thickness-dependent (a) current–potential curves and (b) photocurrent densities at 1.23 V_{RHE} on the WO_3 photoanodes synthesized at 650°C. The electrodes were illuminated from the front side, the electrolyte was a 1 mol L^{-1} H_2SO_4 aqueous solution, and the scan rate was 30 mV s^{-1}. (c) Cross-sectional SEM image of the WO_3 650 photoanode (4 layers) showing the WO_3 layers are smooth on the micrometer scale.

may lead to an insufficient/inhomogeneous esterification reaction within the thin precursor solution layer, thereby yielding relatively inhomogeneous particle sizes (Fig. 4d and e). While the fumaric acid concentration determines the amount of the resulting organic ester template, the deficiency of fumaric acid actually weakens the confinement effects on the WO_3 particles (Fig. 5c). Excessive amounts of fumaric acid lead to the formation of larger WO_3 particles, which is suggested to derive from additional heating associated with the presence of high organic fuel content from the ester template (Fig. 5d and e).

The fabrication scheme for WO_3 photoanodes herein is noted to be highly reproducible. The photocurrent-potential curves collected from 50 randomly selected electrodes were statistically analyzed (Fig. 6a). As observed from Fig. 6b and Fig. S6, average photocurrent densities of 1.8 and 2.06 mA cm^{-2} were achieved at 1.23 and 1.8 V_{RHE}, respectively, with small standard deviations. Among these efficient WO_3 650 photoanodes, the optimized photoanode delivered photocurrent densities of ca. 2.05 and 2.23 mA cm^{-2} at 1.23 and 1.8 V_{RHE}, respectively (Fig. 6c). Additionally, the effectiveness of the present AMT-based precursor solution was maintained for at least 3 weeks, as compared with the associated upper-limit values after 3 d in the presence of peroxytungstic acid- and tungstic acid-based precursors. After aging for 110 d, the AMT-based precursor solution could still be used to fabricate efficient WO_3 photoanodes, with a slight decrease in photoactivity (Fig. S7).

Photocurrent action spectra and photostability of the WO_3 650 photoanode

A previous report suggested that the use of CH_3SO_3H as the electrolyte promoted WO_3 photoanodes to generate large and stable photocurrents when compared with commonly applied H_2SO_4 [49,50]. Fig. 6c displays the photocurrent–potential profiles of the optimized WO_3 650 photoanode when immersed in 1 mol L^{-1} H_2SO_4 and CH_3SO_3H solutions. As expected, the photocurrent densities of the optimized WO_3 650 increased from 2.05 to 2.25 mA cm^{-2} at 1.23 V_{RHE}, and from 2.23 to 2.4 mA cm^{-2} at 1.8 V_{RHE}, when switching the electrolyte from H_2SO_4 to CH_3SO_3H; the onset potential of the optimized WO_3 650

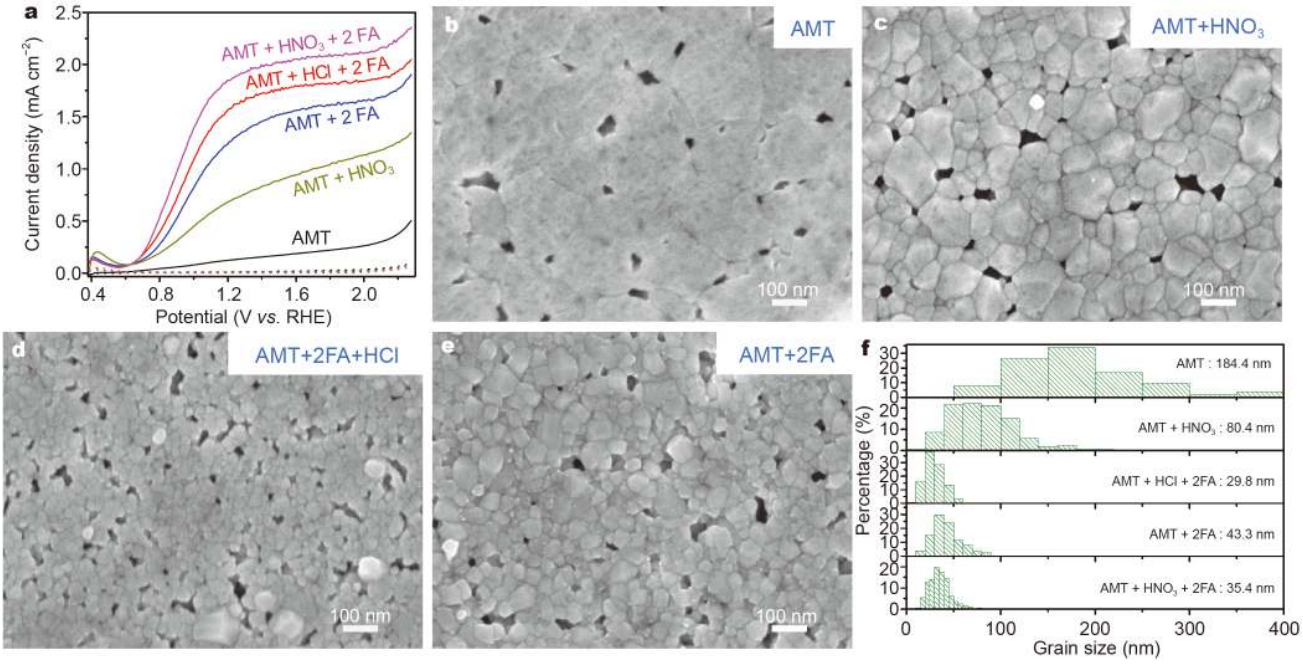

Figure 4 PEC and morphological properties of the WO_3 photoanodes synthesized from different precursor solution compositions. (a) Precursor solution-dependent current–potential curves of the WO_3 photoanodes synthesized at 650°C. The electrodes were illuminated from the front side, the electrolyte was a 1 mol L^{-1} H_2SO_4 aqueous solution, and the scan rate was 30 mV s^{-1}. (b–f) SEM images, grain size distributions and mean grain sizes of the WO_3 films synthesized from different precursor solution compositions. AMT: ammonium metatungstate; FA: fumaric acid.

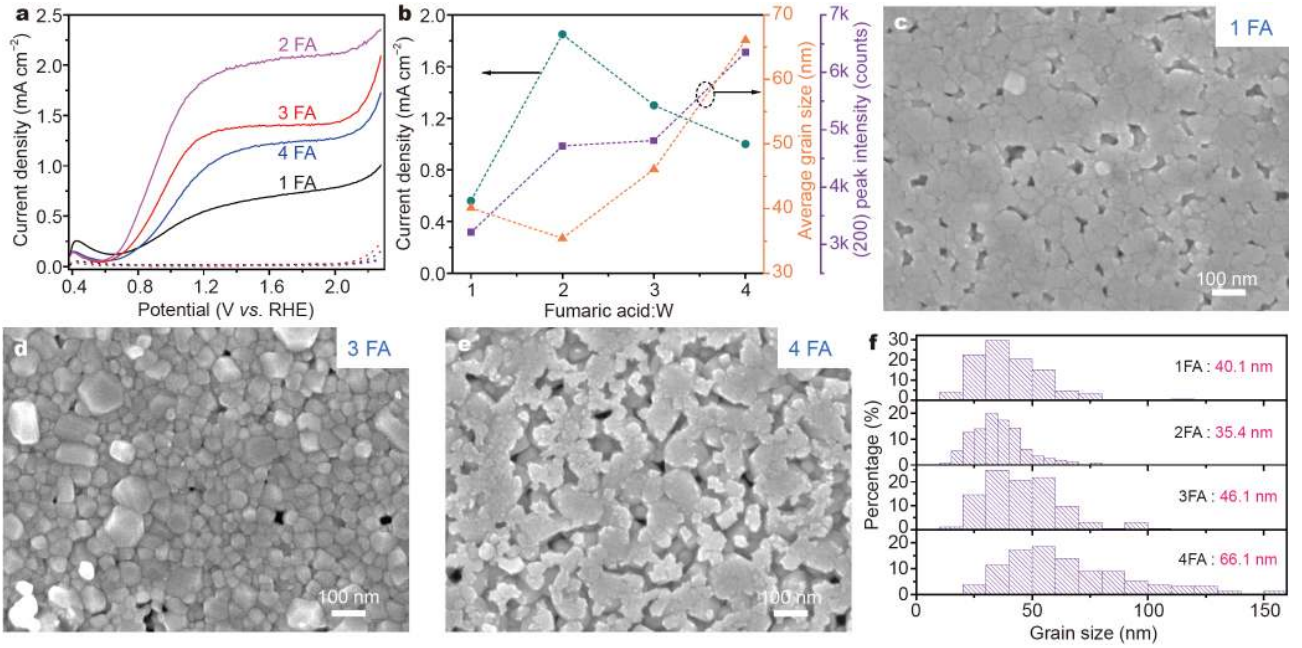

Figure 5 PEC and morphological properties of the WO_3 photoanodes synthesized from different fumaric acid concentrations. Fumaric acid concentration-dependent (a) current–potential curves and (b) photocurrent densities at 1.23 V_{RHE} on the WO_3 photoanodes synthesized at 650°C. Average grain sizes and (200) peak intensities of the WO_3 photoanodes as a function of fumaric acid concentration are also shown for comparison. The electrodes were illuminated from the front side, the electrolyte was a 1 mol L^{-1} H_2SO_4 aqueous solution, and the scan rate was 30 mV s^{-1}. (c–f) SEM images, grain size distributions and mean grain sizes of the WO_3 films synthesized from different fumaric acid concentrations.

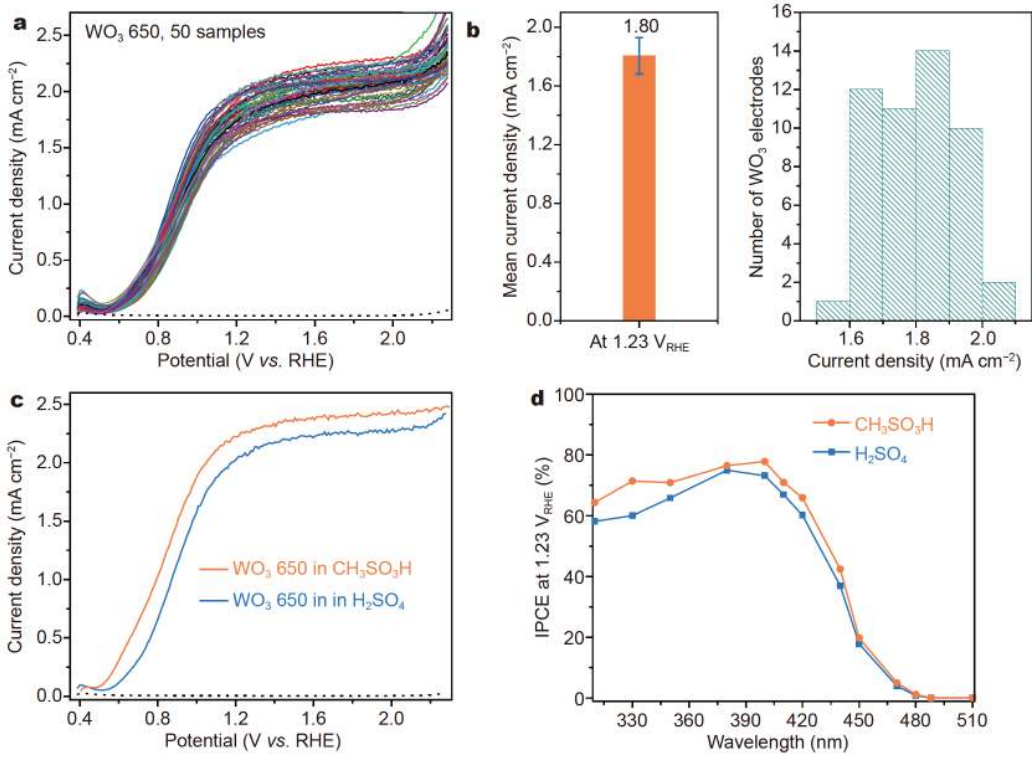

Figure 6 The reproducibility and photocurrent action spectra of WO_3 650 photoanodes. (a) Current–potential curves of 50 pieces of WO_3 650 photoanodes. (b) Mean photocurrent density with the standard deviation (0.12 mA cm^{-2}) and the histogram of photocurrent densities at 1.23 V_{RHE} for 50 pieces of WO_3 650 photoanodes. The electrodes were illuminated from the front side, the electrolyte was a 1 mol L^{-1} H_2SO_4 aqueous solution, and the scan rate was 30 mV s^{-1}. (c) Current–potential curves and (d) IPCE spectra of the champion WO_3 650 photoanode (4 layers) in 1 mol L^{-1} H_2SO_4 and CH_3SO_3H solutions. The electrodes were illuminated from the front side, and the scan rate was 30 mV s^{-1}.

was also observed to shift toward the cathodic side by 80–100 mV, indicating an accelerated surface charge transfer process.

IPCE spectra of the optimized WO_3 650 photoanode at 1.23 V_{RHE} were measured in H_2SO_4 and CH_3SO_3H solutions. As shown in Fig. 6d, replacing H_2SO_4 with CH_3SO_3H improved the overall profile of the photocurrent action spectrum for the optimized WO_3 650 as a result of a faster surface-hole transfer rate in CH_3SO_3H. Both IPCE curves exhibited an onset wavelength of ca. 470 nm, consistent with the bandgap value of 2.6 eV for monoclinic WO_3. From ca. 450 nm, the IPCE curves exhibited a sharp increase toward the UV range, with the highest IPCE values appearing at ~380 nm for the H_2SO_4 electrolyte and 400 nm for the CH_3SO_3H electrolyte, reaching 74.9% and 77.8%, respectively. For photons having wavelengths of <380 nm, both IPCE curves decayed gradually, which can be rationalized by the shallow penetration depths of these photons that hinder efficient electron collection. The high IPCE values on the optimized WO_3 650 photoanode guarantee an appreciable water splitting performance, despite a limited utilization of the solar spectrum into the blue portion of the visible light region. The integrated photocurrent values for the optimized WO_3 650 in H_2SO_4 and CH_3SO_3H solutions, calculated from the IPCE curves and standard solar spectral distributions, are 2.17 and 2.37 mA cm^{-2} at 1.23 V_{RHE}, respectively (Fig. S8). The good agreement between the predicted photocurrents and the measured values validates the reliability of the IPCE values and acquired photocurrents in the present study.

A brief summary of previously reported PEC performances for highly efficient WO_3 photoanodes (without heterojunctions or surface modifications) is provided in Table S1, which shows that the photocurrents associated with the optimized WO_3 650 photoanode are not sufficiently large. A poor hole-transfer process at the WO_3–electrolyte interface, the lack of appropriate film porosity, and defects formed at the WO_3–FTO interface may largely suppress the activity of the WO_3 650 photoanodes. Correspondingly, depositing functional overlayers [51,52] and underlayers [48], and constructing nanostructured/

porous electrodes [23,28–32] may achieve highly efficient solar energy conversions.

Finally, the photostability of the WO_3 650 photoanode (active area = 0.5 cm^2) was tested at 1.23 V_{RHE} in 1 mol L^{-1} H_2SO_4. After 10-h irradiation, the photocurrent of WO_3 650 decreased from ca. 1.9 to 0.4 mA cm^{-2}. Subjecting the WO_3 650 photoanode to darkness for 70 s, followed by illuminating again failed to restore the photocurrent (Fig. S9). Instead, performing cyclic voltammetry toward the negative direction (from 0 to −0.1 V *vs.* Ag/AgCl) fully restored the initial photoactivity, while the gradual decrease in photocurrent remained. Previous studies have ascribed this decline of photoactivity observed on the WO_3 photoanodes to the formation and accumulation of surface tungsten peroxo species, which leads to surface deactivation and slow dissolution of WO_3 [36,48]. After 10-h irradiation, 0.063 mg L^{-1} of dissolved W was detected in the H_2SO_4 electrolyte by inductively coupled plasma-atomic emission spectroscopy measurements. Therefore, further improvements of the photostability on the WO_3 photoanodes are also necessary to assemble the photoanodes into efficient PEC water-splitting devices.

CONCLUSIONS

Prior to this study, the production of highly reproducible and efficient WO_3 photoanodes was complicated by the ever-changing structures/compositions and chemical environments of the applied precursor solutions, comprising peroxytungstic acid and tungstic acid. To circumvent this long-standing challenge, a modified sol-gel process was developed in which chemically stable AMT was used as the precursor. Under simulated sunlight the optimized WO_3 photoanode exhibited photocurrent densities of ca. 2.05 and 2.25 mA cm^{-2} at 1.23 V_{RHE} in 1 mol L^{-1} H_2SO_4 and CH_3SO_3H, respectively, which confirms the WO_3 photoanode as one of the WO_3 photoanodes with the highest performance ever reported. Statistical analysis of the PEC performances on 50 randomly selected WO_3 films yielded an average photocurrent density of 1.8 mA cm^{-2} at 1.23 V_{RHE} in 1 mol L^{-1} H_2SO_4 with a small standard deviation, demonstrating the high reproducibility of the present fabrication scheme for WO_3 photoanodes. Additionally, the AMT-based precursor solution maintained an effective environment to produce efficient WO_3 photoanodes for 3 weeks, when compared with the associated values after 3 d in the presence of peroxytungstic acid- and tungstic acid-based precursors. This study provides a facile and yet effective strategy to fabricate WO_3 photoanodes, which would boost the use of this prototypical photoanode material for highly efficient PEC water-splitting devices.

Received 10 April 2020; accepted 10 June 2020; published online 11 September 2020

1 Montoya JH, Seitz LC, Chakthranont P, *et al.* Materials for solar fuels and chemicals. Nat Mater, 2017, 16: 70–81
2 Sivula K, van de Krol R. Semiconducting materials for photoelectrochemical energy conversion. Nat Rev Mater, 2016, 1: 15010
3 Wu D, Hu S, Xue H, *et al.* Protonation and microwave-assisted heating induced excitation of lone-pair electrons in graphitic carbon nitride for increased photocatalytic hydrogen generation. J Mater Chem A, 2019, 7: 20223–20228
4 Dai B, Yu Y, Chen Y, *et al.* Construction of self-healing internal electric field for sustainably enhanced photocatalysis. Adv Funct Mater, 2019, 29: 1807934
5 Gao H, Guo Y, Yu Z, *et al.* Incorporating *p*-phenylene as an electron-donating group into graphitic carbon nitride for efficient charge separation. ChemSusChem, 2019, 12: 4285–4292
6 Fujishima A, Honda K. Electrochemical photolysis of water at a semiconductor electrode. Nature, 1972, 238: 37–38
7 Feng J, Huang H, Fang T, *et al.* Defect engineering in semiconductors: manipulating nonstoichiometric defects and understanding their impact in oxynitrides for solar energy conversion. Adv Funct Mater, 2019, 29: 1808389
8 Chu S, Vanka S, Wang Y, *et al.* Solar water oxidation by an InGaN nanowire photoanode with a bandgap of 1.7 eV. ACS Energy Lett, 2018, 3: 307–314
9 Fang T, Huang H, Feng J, *et al.* Exploring facile strategies for high-oxidation-state metal nitride synthesis: carbonate-assisted one-step synthesis of Ta_3N_5 films for solar water splitting. Sci Bull, 2018, 63: 1404–1410
10 Pei L, Xu Z, Shi Z, *et al.* Mg-doped Ta_3N_5 nanorods coated with a conformal CoOOH layer for water oxidation: bulk and surface dual modification of photoanodes. J Mater Chem A, 2017, 5: 20439–20447
11 Xu Z, Guan Z, Yang J, *et al.* Band positions and photoelectrochemical properties of solution-processed silver-substituted Cu_2ZnSnS_4 photocathode. ACS Appl Energy Mater, 2019, 2: 2779–2785
12 Zhao X, Hu J, Wu B, *et al.* Simultaneous enhancement in charge separation and onset potential for water oxidation in a $BiVO_4$ photoanode by W–Ti codoping. J Mater Chem A, 2018, 6: 16965–16974
13 Hu Y, Wu Y, Feng J, *et al.* Rational design of electrocatalysts for simultaneously promoting bulk charge separation and surface charge transfer in solar water splitting photoelectrodes. J Mater Chem A, 2018, 6: 2568–2576
14 Xu Z, Fan Z, Shi Z, *et al.* Interface manipulation to improve plasmon-coupled photoelectrochemical water splitting on α-Fe_2O_3 photoanodes. ChemSusChem, 2018, 11: 237–244
15 Zhang N, Zheng H, Guo Y, *et al.* Design principles for construction of charge transport channels in particle-assembled water-splitting photoelectrodes. ACS Sustain Chem Eng, 2019, 7: 10509–10515
16 Pan L, Kim JH, Mayer MT, *et al.* Boosting the performance of Cu_2O photocathodes for unassisted solar water splitting devices. Nat Catal, 2018, 1: 412–420
17 Mao G, Xu M, Yao S, *et al.* Direct growth of Cr-doped TiO_2

nanosheet arrays on stainless steel substrates with visible-light photoelectrochemical properties. New J Chem, 2018, 42: 1309–1315
18 Feng J, Wang Z, Zhao X, *et al.* Probing the performance limitations in thin-film $FeVO_4$ photoanodes for solar water splitting. J Phys Chem C, 2018, 122: 9773–9782
19 Zhang N, Wang X, Feng J, *et al.* Paving the road toward the use of β-Fe_2O_3 in solar water splitting: Raman identification, phase transformation and strategies for phase stabilization. Natl Sci Rev, 2020, 7: 1059–1067
20 Mi Q, Zhanaidarova A, Brunschwig BS, *et al.* A quantitative assessment of the competition between water and anion oxidation at WO_3 photoanodes in acidic aqueous electrolytes. Energy Environ Sci, 2012, 5: 5694–5700
21 Feng J, Zhao X, Ma SSK, *et al.* Fast and simple construction of efficient solar-water-splitting electrodes with micrometer-sized light-absorbing precursor particles. Adv Mater Technol, 2016, 1: 1600119
22 Cao D, Wang J, Zhang J, *et al.* Mechanism investigation of the postnecking treatment to WO_3 photoelectrodes. ACS Appl Energy Mater, 2018, 1: 4670–4677
23 Santato C, Odziemkowski M, Ulmann M, *et al.* Crystallographically oriented mesoporous WO_3 films: Synthesis, characterization, and applications. J Am Chem Soc, 2001, 123: 10639–10649
24 Marsen B, Miller EL, Paluselli D, *et al.* Progress in sputtered tungsten trioxide for photoelectrode applications. Int J Hydrogen Energy, 2007, 32: 3110–3115
25 Kalanur SS, Hwang YJ, Chae SY, *et al.* Facile growth of aligned WO_3 nanorods on FTO substrate for enhanced photoanodic water oxidation activity. J Mater Chem A, 2013, 1: 3479–3488
26 Zhang J, Zhang P, Wang T, *et al.* Monoclinic WO_3 nanomultilayers with preferentially exposed (002) facets for photoelectrochemical water splitting. Nano Energy, 2015, 11: 189–195
27 Amano F, Li D, Ohtani B. Fabrication and photoelectrochemical property of tungsten(VI) oxide films with a flake-wall structure. Chem Commun, 2010, 46: 2769–2771
28 Li W, Da P, Zhang Y, *et al.* WO_3 nanoflakes for enhanced photoelectrochemical conversion. ACS Nano, 2014, 11: 11770–11777
29 Su J, Feng X, Sloppy JD, *et al.* Vertically aligned WO_3 nanowire arrays grown directly on transparent conducting oxide coated glass: Synthesis and photoelectrochemical properties. Nano Lett, 2011, 11: 203–208
30 Wang G, Ling Y, Wang H, *et al.* Hydrogen-treated WO_3 nanoflakes show enhanced photostability. Energy Environ Sci, 2012, 5: 6180–6187
31 Chen Q, Li J, Zhou B, *et al.* Preparation of well-aligned WO_3 nanoflake arrays vertically grown on tungsten substrate as photoanode for photoelectrochemical water splitting. Electrochem Commun, 2012, 20: 153–156
32 Ma M, Zhang K, Li P, *et al.* Dual oxygen and tungsten vacancies on a WO_3 photoanode for enhanced water oxidation. Angew Chem Int Ed, 2016, 55: 11819–11823
33 Li Z, Feng J, Yan S, *et al.* Solar fuel production: Strategies and new opportunities with nanostructures. Nano Today, 2015, 10: 468–486
34 Wang Y, Tian W, Chen C, *et al.* Tungsten trioxide nanostructures for photoelectrochemical water splitting: Material engineering and charge carrier dynamic manipulation. Adv Funct Mater, 2019, 29: 1809036
35 Li L, Xiao S, Li R, *et al.* Nanotube array-like WO_3 photoanode with dual-layer oxygen-evolution cocatalysts for photoelectrocatalytic overall water splitting. ACS Appl Energy Mater, 2018, 1: 6871–6880
36 Seabold JA, Choi KS. Effect of a cobalt-based oxygen evolution catalyst on the stability and the selectivity of photo-oxidation reactions of a WO_3 photoanode. Chem Mater, 2011, 23: 1105–1112
37 Zhao Y, Yan X, Yang KR, *et al.* End-on bound iridium dinuclear heterogeneous catalysts on WO_3 for solar water oxidation. ACS Cent Sci, 2018, 4: 1166–1172
38 Rashad MM, Shalan AE. Hydrothermal synthesis of hierarchical WO_3 nanostructures for dye-sensitized solar cells. Appl Phys A, 2014, 116: 781–788
39 Biswas SK, Baeg JO, Moon SJ, *et al.* Morphologically different WO_3 nanocrystals in photoelectrochemical water oxidation. J Nanopart Res, 2012, 14: 667
40 Hong SJ, Jun H, Borse PH, *et al.* Size effects of WO_3 nanocrystals for photooxidation of water in particulate suspension and photoelectrochemical film systems. Int J Hydrogen Energy, 2009, 34: 3234–3242
41 Patil PS, Patil PR, Ennaoui EA. Characterization of ultrasonic spray pyrolyzed tungsten oxide thin films. Thin Solid Films, 2000, 370: 38–44
42 Yang H, Shang F, Gao L, *et al.* Structure, electrochromic and optical properties of WO_3 film prepared by dip coating-pyrolysis. Appl Surf Sci, 2007, 253: 5553–5557
43 Go GH, Shinde PS, Doh CH, *et al.* PVP-assisted synthesis of nanostructured transparent WO_3 thin films for photoelectrochemical water splitting. Mater Des, 2016, 90: 1005–1009
44 Jin GH, Liu SQ. Effect of substrates on crystal structures and optical properties of WO_3 films prepared by the polymeric precursor method. Dig J Nanomater Bios, 2016, 11: 763–771
45 Yano M, Iwata T, Murakami S, *et al.* Gas sensing characteristics of a WO_3 thin film prepared by a sol-gel method. Proceedings, 2018, 2: 723
46 Brillet J, Gratzel M, Sivula K. Decoupling feature size and functionality in solution-processed, porous hematite electrodes for solar water splitting. Nano Lett, 2010, 10: 4155–4160
47 Feng J, Luo W, Fang T, *et al.* Highly photo-responsive $LaTiO_2N$ photoanodes by improvement of charge carrier transport among film particles. Adv Funct Mater, 2014, 24: 3535–3542
48 Liang Y, Tsubota T, Mooij LPA, *et al.* Highly improved quantum efficiencies for thin film $BiVO_4$ photoanodes. J Phys Chem C, 2011, 115: 17594–17598
49 Solarska R, Jurczakowski R, Augustynski J. A highly stable, efficient visible-light driven water photoelectrolysis system using a nanocrystalline WO_3 photoanode and a methane sulfonic acid electrolyte. Nanoscale, 2012, 4: 1553–1556
50 Bignozzi CA, Caramori S, Cristino V, *et al.* Nanostructured photoelectrodes based on WO_3: applications to photooxidation of aqueous electrolytes. Chem Soc Rev, 2013, 42: 2228–2246
51 Kim W, Tachikawa T, Monllor-Satoca D, *et al.* Promoting water photooxidation on transparent WO_3 thin films using an alumina overlayer. Energy Environ Sci, 2013, 6: 3732–3739
52 Zhang S, Lv F, Zhang X, *et al.* Ni@RuM (M=Ni or Co) core@shell nanocrystals with high mass activity for overall water-splitting catalysis. Sci China Mater, 2019, 62: 1868–1876

Acknowledgements This work was supported by the Ministry of Education (MOE) Tier 1 (M4011959 and M4011528), the National Key Research and Development Program of China (2018YFA0209303), the

National Natural Science Foundation of China (U1663228 and 51902153) and the Project Funded by the Priority Academic Program Development of Jiangsu Higher Education Institutions.

Author contributions Feng J, Zhao X, Li Z and Huang Y designed the research; Feng J, Zhao X, Zhang B, Yang G, Qian Q, and Ma S fabricated the samples, performed the current–potential curve, XRD, ultraviolet–visible spectra, SEM and IPCE measurements; all the authors discussed the results and co-wrote the paper.

Conflict of interest The authors declare that they have no conflict of interest.

Supplementary information Supporting data are available in the online version of the paper.

Jianyong Feng obtained his PhD at Nanjing University in 2014, then he worked as a postdoctoral fellow at Nanyang Technological University, Singapore. Since 2017, he has been a research scientist at the College of Engineering and Applied Sciences, Nanjing University. His research interests are photoelectrochemical water splitting and solar cells.

Xin Zhao received his BSc from China Agricultural University in 2009, and PhD from Nanjing University in 2014, respectively. He joined the School of Materials Science and Engineering at Nanyang Technological University as a research fellow in 2014, working with Prof. Zhong Chen, and then moved to the School of Physical & Mathematical Sciences with Dr. Han Sen Soo. His current interests include photoluminescence, photoelectrochemistry for solar energy conversion, earth-abundant elements to valorize biomass lignin and degrade environmental pollutants by ambient condition C–C bond activation.

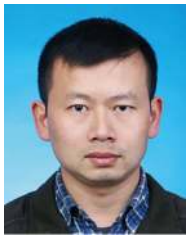

Zhaosheng Li received his PhD in condensed matter physics from the Institute of Solid State Physics, Chinese Academy of Sciences, China, in 2003. After a two-year postdoctoral fellowship at Nanjing University, he became a lecturer at this university. In 2006, he was promoted to an Associate Professor of materials science and engineering at Nanjing University. Since Dec 2011, he has become a full Professor of materials science and engineering at the College of Engineering and Applied Sciences, Nanjing University. His current research interests are photoelectrochemistry and photocatalysis.

Yizhong Huang is currently positioned in the School of Materials Science and Engineering at Nanyang Technological University in Singapore. He has been working in the University of Oxford as a postdoc and then research fellow (faculty member) and college fellow of Wolfson and now an academic visitor. He has developed his expertise in transmission electron microscopy (TEM) and focused ion beam (FIB) system with specific research interests in nano-electrochemistry and hybrid nanostructured materials for energy applications.

溶胶-凝胶法制备高重复性的WO_3光阳极用于太阳能水氧化反应

冯建勇[1†], 赵新[1†], 张博威[1], 杨光[1], 钱勤枫[2], 马苏苏[1], 陈忠[1], 李朝升[2*], 黄一中[1*]

摘要 单斜相WO_3是一种用于太阳能水分解反应的经典光阳极材料, 但如何可靠地制备高效WO_3光阳极仍具有挑战性. 这主要是由于常用的过氧钨酸及新制钨酸前驱体的成分/结构及化学环境不断变化, 使得后续的制备过程不可控. 本文报道了一种以化学稳定性好的偏钨酸铵作为前驱体的溶胶-凝胶策略, 可获得高效、高重复性的WO_3光阳极. 结果表明在模拟太阳光辐照下最优WO_3光阳极在可逆氢电极1.23 V处可产生2.05与2.25 mA cm^{-2}(1 mol L^{-1} H_2SO_4及CH_3SO_3H中)的光电流. 随机选择的50片WO_3光阳极于1 mol L^{-1} H_2SO_4中的测试结果表明在1.23 V处的光电流平均值为1.8 (±0.12) mA cm^{-2}. 此外, 偏钨酸铵前驱体溶液可持续生效至少三周, 而过氧钨酸及新制钨酸前驱体的有效时间不超过三天. 本研究为构建高效WO_3光阳极提供了新的研究思路与实验基础.

